

The manifold rheology of fluidized granular media

Olfa D'Angelo^{a,b,1}, Abhishek Shetty^c, Matthias Sperr^{b,d}, and W. Till Kranz^{d,b}

^aInstitute for Multiscale Simulation, Erlangen-Nürnberg Universität, Cauerstraße 3, 91058 Erlangen, Germany; ^bInstitute of Materials Physics in Space, German Aerospace Center (DLR), Linder Höhe, 51170 Cologne, Germany; ^cRheology Department, Anton Paar USA, Inc., 10215 Timber Ridge Drive, Ashland, VA 23005, United States of America; ^dInstitute for Theoretical Physics, University of Cologne, 50937 Cologne, Germany

This manuscript was compiled on September 4, 2023

Fluidized granular media have a rich rheology: measuring shear stress σ as a function of shear rate $\dot{\gamma}$, they exhibit Newtonian behavior $\sigma \sim \dot{\gamma}$ for low densities and shear rates, develop a yield stress for intermediate shear rates and densities approaching the granular glass transition, and finally, cross over to shear-thickening Bagnold scaling, $\sigma \sim \dot{\gamma}^2$. This wealth of flow-behaviors makes fluidized beds a fascinating material, but also one that is challenging to encompass into a global theory, despite its relevance for optimizing industrial processes and predicting natural hazards. We provide careful measurements spanning eight orders of magnitude in shear rate, and show that all these rheological regimes can be described qualitatively and quantitatively using the granular integration through transient formalism, a theory for glassy dynamics under shear adapted to granular fluids.

Fluidized bed | Rheology | Non-Newtonian Fluid | Integration Through Transients

Fluidization counteracts the dissipative nature of granular materials by a constant energy input (1–4). Transforming static granular solids into dynamic granular fluids, fluidization maintains a non-zero mean kinetic energy per particle, i.e., a finite granular temperature T (5). The macroscopic solid particles that collectively constitute the granular medium may be agitated by a number of external forces, including an interstitial fluid pressure in gas-fluidized media (6–9), shaking in vibro-fluidization (10–12), pressure waves in acoustic fluidization (13, 14).

In most natural and human-made processes involving granular fluids, fluidization and shear happen simultaneously. Typical examples in geophysical flows (7, 9, 13, 15, 16) are avalanches, land slides, pyroclastic flows – all natural hazards threatening human lives. Two-phase flows of a non-Brownian solid phase of macroscopic particles in a molecular fluid are also a common industrial system, e.g. in fluid-particles mixing (17), fluidized bed reactors (18, 19), or pneumatic conveyors (20).

Despite the critical importance of fluidized granular media under shear for process optimization and risk mitigation, studies of their rheology remain sparse and produce seemingly conflicting results. Some studies find Newtonian rheology (21–24), some shear thinning (25, 26), and some Bagnold rheology (27). Other studies found crossovers between these (8, 28–32). We will show below that, in fact, the fluidized bed rheology comprises all three rheological behaviors: Newtonian, shear thinning, and Bagnoldian. For the Bagnold regime (33, 34) alone, the empirical $\mu(T)$ -rheology (35) has been very successful. However, a succinct and comprehensive constitutive equation describing agitated granular fluids – stress tensor Σ as a function of shear rate $\dot{\gamma}$ – remains hitherto missing.

We carefully measure the steady-state rheology of gas-fluidized glass beads, treating the fluidized bed as an effectively homogeneous material, and measuring the macroscopic mean shear stress σ as a function of shear rate $\dot{\gamma}$, in a wide-gap

Taylor-Couette shear cell (36). By spanning eight orders of magnitude in shear rates, we delineate a diversity of rheological regimes. Using a glassy dynamics theory, the granular integration through transient (g-ITT) formalism as recently proposed by some of us as a constitutive model, derived from first principles (37, 38), we fit the experimental flow curves. Using a minimal number of physically meaningful fit parameters, all rheological regimes are encompassed in the theoretical prediction. Finding that the fit parameters are consistent among different flow curves, we thereby also validate the g-ITT constitutive relation.

Gas-fluidized granular media under shear

Fluidized bed. Gas-fluidized granular fluids are a challenging material for a number of reasons. They are a genuine two-phase material, composed of the macroscopic solid particles that constitute the granular phase and the molecular fluid surrounding them (39–41). Stokes numbers are $\mathcal{O}(10)$, such that the particles are neither completely over-damped and enslaved by the molecular fluid (40), nor can the molecular fluid's viscosity, η_f , be neglected to treat the material as a granular gas of particles only. As the particles are macroscopic, they are athermal, i.e. their kinetic energy is not in equilibrium with the thermal energy of the molecular fluid. Nevertheless, as the gas flow maintains the grains' motion, a finite mean kinetic energy per particle can be associated with any granular fluid, i.e., a finite granular temperature $T > 0$, unrelated to the thermodynamic temperature. The energy injected by fluidization is constantly dissipated in particle collisions,

Significance Statement

From industrial reactors to geophysical flows, fluidized granular media under shear are widespread, yet poorly understood from a fundamental point of view. Combining rheological measurements on air-fluidized glass beads spanning eight orders of magnitude in shear rate, with a glassy dynamics theory based on first-principles, we confirm and explain rheological regimes in agitated granular beds: Newtonian, shear thinning, and Bagnoldian shear thickening regimes. Such carefully measured rheology provides essential ground-truth for future studies, notably to predict pyroclastic flows and avalanches. It is also a step towards a universal theoretical description of granular flows.

M.S.: conceptualization; project administration; validation; resources; writing - review & editing. W. T. Kranz: conceptualization; formal analysis; methodology; validation; supervision; writing - original draft. O.D.A.: conceptualization; data curation; investigation; formal analysis; methodology; project administration; visualization; writing - original draft. A.S.: resources; data curation; writing - review & editing.

The authors declare no conflict of interest.

¹To whom correspondence should be addressed. E-mail: olfa.dangelo@fau.de

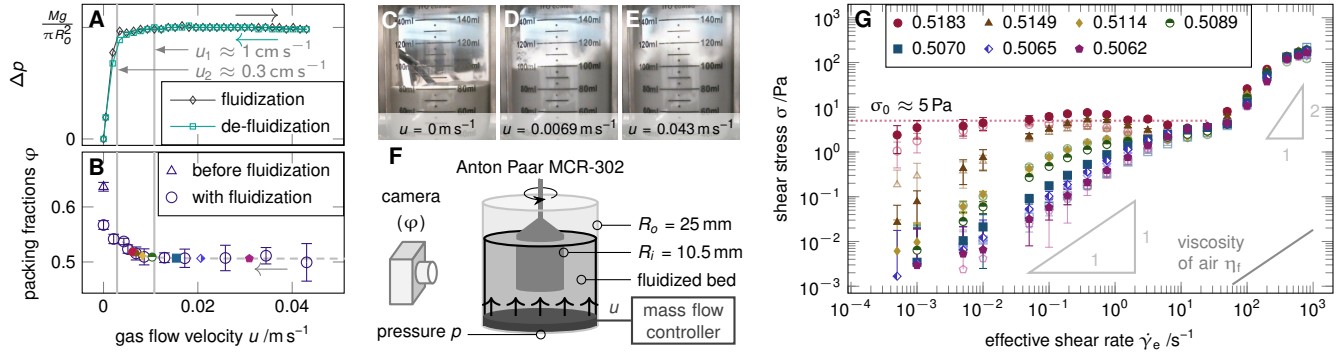


Fig. 1. Fluidization and flow curves of air-fluidized glass beads. (A) Air pressure drop across the powder bed, Δp , due to the flow resistance of the granular bed, as a function of superficial fluidization velocity u , for decreasing (green squares) followed by increasing (gray diamonds) air flow velocity u . (B) Global packing fraction φ as a function of air flow velocity u (colored symbols indicate the flow velocities selected for further investigation, same color coding as in Fig. 1G – see legend there for packing fraction values). Error bars correspond to the volume fluctuation due to bubbling. Vertical lines in (A, B) indicate the lower and upper bounds of the fluidization range (respectively u_2 and u_1). (C, D, E) Pictures of the powder bed at increasing air flow velocity, from left to right: $u = 0 \text{ cm s}^{-1}$ (before fluidization), $u = 0.69 \text{ cm s}^{-1}$ and $u = 4.3 \text{ cm s}^{-1}$. (F) Schematic of the wide-gap Taylor-Couette rheometry setup: Anton Paar MCR 302 with commercial powder flow cell and profiled cylinder (see Methods for details), and camera recording the global powder bed volume. (G) Macroscopic stress σ as a function of effective shear rate $\dot{\gamma}_e$ for the air flow velocities indicated in (B). Each mark shape and color represent one air flow velocity u ; equivalent φ are given as legend. Filled marks represent the upward sweep, empty marks represent downward sweep in $\dot{\gamma}_e$. Error bars are the standard deviation on all data points measured in steady state. The shear stress due to air alone is indicated by the gray line at the bottom right of the graph. Triangles at low and high shear rates indicate the slopes of Newtonian and Bagnold behavior, respectively. Dotted red horizontal line indicates the yield stress of the partially fluidized bed at $\sigma_0 \approx 5 \text{ Pa}$.

making granular fluids by nature out of equilibrium.

We focus on a fluidized bed of glass beads of mean diameter $d = 69 \mu\text{m}$ (Geldart group A (1), see Methods for details and Refs. (31, 42) for further characterization), and vary the fluidization velocity u . To characterize the fluidization state, we monitor the pressure drop Δp across the particle bed (Fig. 1A). While we find the bed to be fully fluidized at $u > u_1$ ($Mg = \Delta p \pi R_0^2$, with sample mass $M = 125 \text{ g}$, the gravitational acceleration g , and a container of radius R_0), it is already partially fluidized at $u_1 > u > u_2$, as fluidization occurs across a fluidization range (43). We observe only a small pressure overshoot in the fluidization *versus* defluidization curve around u_1 , which indicates minimal cohesion between particles (44).

By recording the time-averaged mean bed height (Figs. 1C–E), we determine the global packing fraction $\varphi(u)$ corresponding to a given fluidization velocity u (see Fig. 1B and Methods). Starting in the partially fluidized regime and reaching deep into the fully fluidized state, we select seven representative fluidization states – or packing densities – for further investigation. Note that we report the packing fractions to a much higher precision than is warranted by the measurement’s accuracy to reflect the monotonicity of $\varphi(u)$ (45). The superficial fluidization velocity u remains the primary control parameter. At the higher fluidization velocities, we observe significant bubbling (1, 45). However, by time-averaging, we treat the fluidized bed, including bubbles, as an effectively homogeneous material.

Rheometry. We measure the steady-state macroscopic shear stress $\sigma(\dot{\gamma}_e)$ of air-fluidized glass beads, as a function of effective shear rate $\dot{\gamma}_e$. An Anton Paar MCR 302 rheometer with Taylor-Couette geometry is used in shear-rate controlled mode (see Fig. 1F and Methods for technical details). Fig. 1G shows the resulting flow curves (see Methods for full experimental procedure); σ is time-averaged per $\dot{\gamma}_e$, and for every packing fraction, we measured the curves both in an up-sweep and down-sweep in shear rate. We call effective shear rate the shear rate as calculated for a purely Newtonian fluid experiencing uniform shear across the entire gap, i.e., $\dot{\gamma}_e := 2\pi K_N U$, lin-

early related to the rotation rate of the inner cylinder U by the shear constant K_N (see Methods for details). For preliminary results with a similar setup see Refs. (8, 46).

We see that irrespective of the bubbling instability, packing fractions are typically high, $\varphi \gtrsim 0.5$, such that a fluidized bed cannot be regarded as a dilute suspension, where the suspended particles merely provide a correction to the molecular fluid’s viscosity η_f . On the contrary, the shear stress is dominated by the particles and orders of magnitude larger than the stress $\eta_f \dot{\gamma}_e$ exerted by air alone.

Rheological Regimes

We observe a complex rheology of the fluidized bed, with regions of the parameter space that appear to be compatible with a Newtonian rheology $\sigma \sim \dot{\gamma}_e$, parts that indicate Bagnold scaling $\sigma \sim \dot{\gamma}_e^2$, and a shear thinning regime where σ appears almost constant. These rheological regimes become more blatant if we plot the shear rate dependent apparent viscosity $\eta_e(\dot{\gamma}_e) \equiv \sigma/\dot{\gamma}_e$ as in Fig. 2A.

Newtonian Regime. At low shear rates and densities, the effective viscosity $\eta_e(\dot{\gamma}_e | \varphi) \simeq \eta_N(\varphi)$ assumes a shear rate independent value that strongly depends on volume fraction, displaying Newtonian rheology (yellow region in Fig. 2A). In Fig. 2B, we plot the viscosity in the Newtonian regime as a function of packing fraction, $\eta_N(\varphi)$ (numerical values given in Tab. 1).

A fit to the following ansatz,

$$\eta_N(\varphi) \propto (\varphi_g - \varphi)^{-\vartheta}, \quad [1]$$

suggests a viscosity diverging towards $\varphi_g = 0.519$, with exponent $\vartheta \approx 2.6$, where we interpret φ_g as the critical packing fraction at the granular glass transition. Note that the value of φ_g (even within the substantial systematic uncertainty of the average volume fraction measurement of $\pm 4.6\%$) could be seen as surprisingly low, if Eq. 1 were to be read as the Krieger-Dougherty relation (47) of colloidal suspensions. Furthermore, interpreted as a close packing density, one would expect φ_g

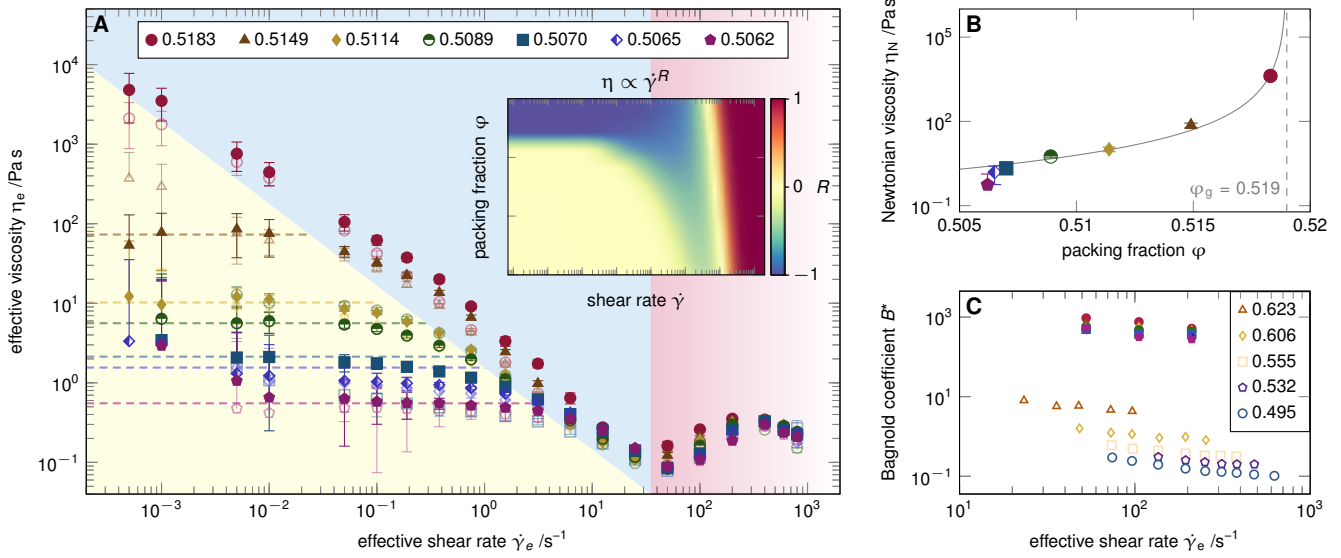


Fig. 2. Experimental rheology of an air-fluidized granular bed. (A) Apparent viscosity, $\eta_e(\dot{\gamma}_e) = \sigma/\dot{\gamma}_e$, as a function of effective shear rate $\dot{\gamma}_e$ for different packing fractions ϕ (see legend). Error bars are the standard deviation on all data points measured in steady state. The different rheological regimes are indicated by the shaded background. Dashed lines indicate the Newtonian viscosities η_N . The inset represents the rheological regimes predicted by granular integration through transient (g-iTT) (see body of text for details), where the color map corresponds to values of R in $\eta \propto \dot{\gamma}^R$. (B) Newtonian viscosities $\eta_N(\phi)$ as a function of packing fraction ϕ . Error bars are standard deviation on all values of $\eta_e(\dot{\gamma})$ within the Newtonian regime. A fit with the law $\eta_N(\phi) \propto (\phi_g - \phi)^{-\vartheta}$ predicts a divergence at the granular glass transition $\phi_g = 0.519$ and $\vartheta = 2.6$. (C) Bagnold coefficients $B = \sigma/\dot{\gamma}^2$ (full symbols) as a function of the effective shear rate $\dot{\gamma}$ and for the different packing fractions (mark shape & color code as in (A)). The lower sets of points (empty symbols) are the Bagnold coefficients extracted from Bagnold's historic measurements, see Ref. (33) (packing fractions indicated in legend).

close to jamming, $\phi_J \approx 0.64$ (or slightly lower given surface friction and polydispersity (48)). However, there is evidence of a granular glass transition, i.e., a dynamically arrested, non-classical granular solid at $T > 0$ (49, 50). Our analysis supports a kinetic granular glass transition (51), where granular mode-coupling theory (g-MCT) (50) predicts Eq. 1 already at a critical density ϕ_g much lower than ϕ_J . We will come back to the value of ϕ_g in the discussion.

Bagnold Regime. At high shear rates $50 \text{ s}^{-1} \lesssim \dot{\gamma}_e \lesssim 350 \text{ s}^{-1}$ (red region in Fig. 2A), $\sigma \sim \dot{\gamma}^2$, exhibiting a shear thickening regime known as Bagnold regime (33).

As the material's flow profile varies with its rheology, the true shear rate is no longer given by $\dot{\gamma}_e$, but related to the turning rate of the inner cylinder, U , as $\dot{\gamma} = K_B 2\pi U$, with the strain constant

$$K_B = \frac{\delta}{\delta - 1}, \quad [2]$$

where $\delta = R_o/R_i$, the ratio of outer to inner radii of the shear cell (full derivation is available as Supplementary Information (SI)).

After the seminal measurements by Bagnold (33), the Bagnold regime and its emergence have been studied repeatedly (52–54), although quantitative measurements of Bagnold coefficients are still scarce. We report in Fig. 2C the resulting Bagnold coefficients $B = \sigma/\dot{\gamma}^2$, in dimensionless form $B^* = Bd/m$ (d and m are respectively the average diameter and mass of one particle). Numerical values of $B(\phi)$ are given in Tab. 1.

We can compare our results with Bagnold's original measurements (33), also plotted in Fig. 2C. The granular suspension in Ref. (33) are wax balls of 1.3 mm diameter, suspended in water or a similar density mixture of glycerin, alcohol and

water. Glass beads being much less dissipative than wax balls, our Bagnold coefficients are orders of magnitude larger than Bagnold's (38, 55).

Table 1. For every air flow velocities u studied: measured global packing fraction ϕ ; average viscosity in the Newtonian regimes η_N (the range of corresponding shear rates is given, calculated for upward sweep in $\dot{\gamma}_e$); Bagnold coefficients B , obtained by averaging $B(\dot{\gamma}_e)$ for all $\dot{\gamma}_e \in [50, 200] \text{ s}^{-1}$.

$u / \text{m s}^{-1}$	ϕ	$\eta_N / \text{Pa s}$	$\dot{\gamma}_e$ range for η_N / s^{-1}	$B / \text{mPa s}^2$
0.0062	0.5183	4200	$5 \cdot 10^{-4}$	4.6
0.0072	0.5149	73	$[5 \cdot 10^{-4}, 0.01]$	3.8
0.0082	0.5114	10	$[5 \cdot 10^{-4}, 0.1]$	3.3
0.010	0.5089	5.6	$[1 \cdot 10^{-3}, 0.1]$	2.9
0.015	0.5070	2.1	$[1 \cdot 10^{-3}, 0.19]$	2.6
0.021	0.5065	1.6	$[5 \cdot 10^{-3}, 0.75]$	2.5
0.031	0.5062	0.55	$[1 \cdot 10^{-2}, 3.13]$	2.3

Shear Thinning Regime. The shear thinning regime is indicated by a blue shading in Fig. 2A and comprises an intermediate range of shear rates that widens towards higher densities. From the corresponding stress plateau in Fig. 1G for our highest density $\phi = 0.5183$, we infer an apparent yield stress $\sigma_0(\phi_g) \approx 5 \text{ Pa}$ at $\phi_g = 0.519$. Note that the emergence of a yield stress at ϕ_g is another manifestation of the fluidized bed's transition from a granular fluid into a granular glassy solid (49–51).

On closer inspection, Figs. 1G and 2A reveal that the flow curves are non-monotonic in the shear thinning regime. Such a phenomenology has been shown to derive from shear banding (56, 57) and is to be expected given the combination

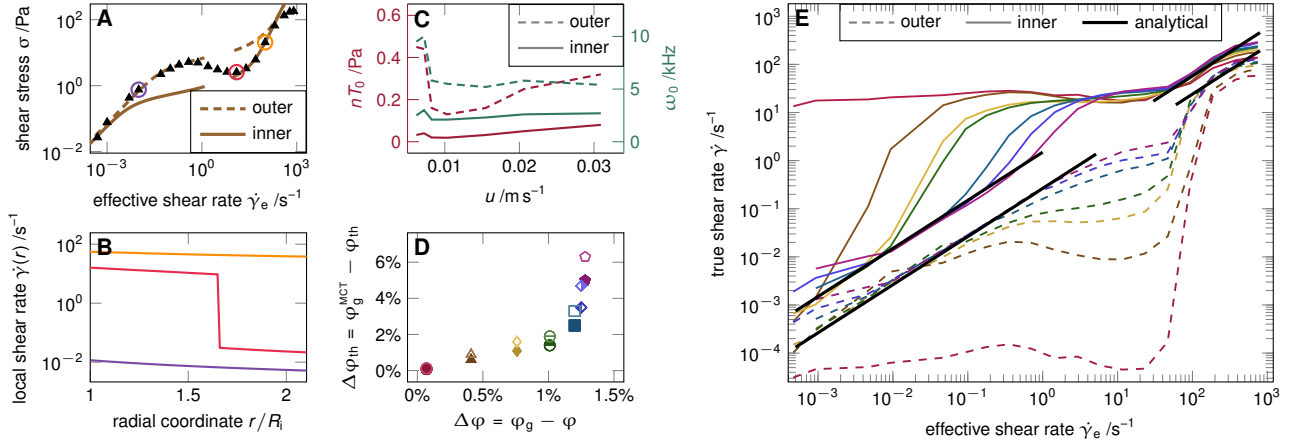


Fig. 3. Shear banding analysis to determine the true shear rate. (A) The non-monotonic experimental flow curves (triangle symbols, here for $u = 0.007 \text{ m s}^{-1}$, see Fig. S2 in SI for all other fluidization speeds) can be fitted to two g-ITT curves, $\sigma^i(\dot{\gamma}_e)$ (inner, solid), and $\sigma^o(\dot{\gamma}_e)$ (outer, dashed), respectively, outside of the negative slope, shear banding regime. (B) True shear rate, $\dot{\gamma}(r)$, as a function of radial coordinate r in the shear cell for three different effective shear rates $\dot{\gamma}_e$ indicated in (A). The lowest (orange) and highest (violet) effective shear rates $\dot{\gamma}_e$ are respectively Newtonian (following σ^o) and Bagnoldian (following σ^i) throughout, while at the intermediate $\dot{\gamma}_e$ (red) the sheared fluid radially separates into a Bagnoldian part near the inner cylinder (following σ^i) and a Newtonian part near the outer cylinder (following σ^o) with a discontinuous step at $r = r^*$. (C) Apparent ideal gas pressure $nT_0(u)$ and apparent collision frequency $\omega_0(u)$ in the unsheared fluidized bed as a function of fluidization velocity u as a result of the g-ITT fit. (D) Distance from the granular glass transition $\Delta\varphi_{\text{th}} = \varphi_g^{\text{MCT}} - \varphi_{\text{th}}$ in the g-ITT fit versus the distance to the granular glass transition $\Delta\varphi$ from the measurements. An effective coefficient of restitution $\varepsilon = 0.8$ with a corresponding $\varphi_g^{\text{MCT}}(\varepsilon = 0.8) = 0.528$ is assumed in (C,D). For other choices of ε see Fig. S9 in SI. (E) Shear rate $\dot{\gamma}$ at the inner cylinder (solid lines) and at the outer cylinder (dashed lines), as a function of the effective shear rate $\dot{\gamma}_e$ for the packing fractions studied. The thick black lines indicate the analytical relations [Eqs. 2,3] in the Newtonian and Bagnold regime. Note the increasing difference between inside and outside in the shear banding regime. For color coded packing fractions in (D, E), refer to Fig. 1G.

of a continuously varying shear stress in the Taylor-Couette geometry and a nearly shear rate independent regime in the constitutive relation. While in the Newtonian and Bagnold regimes, the true shear rate $\dot{\gamma}$ is linearly related to the turning rate U by the strain constants, K_N and K_B , respectively, the mapping $\dot{\gamma}(U)$ is non-linear in the shear thinning, and in particular in the shear banding regime. To find the true shear rate, we numerically analyze shear banding in the next section.

High Shear Rate Regime. At the highest shear rates, a second shear thinning regime seems to establish, clearly visible in Fig. 2A for $\dot{\gamma}_e \geq 400 \text{ s}^{-1}$. Such second viscosity decrease past the shear-thickening Bagnold regime was observed experimentally, albeit rarely, in dense non-Brownian solid-liquid suspensions (58, 59). One possible explanation is that very high shear rates create a pressure gradient in the radial direction, resulting in a strong anisotropy, and in depletion along that direction (59). To the best of our knowledge, it was never observed in dry granular media before.

We propose a similar explanation: the strong azimuthal air flow due to high rotation speed of the corrugated cylinder might create an air cushion between the fluidized bed and the inner cylinder. In other words, the density along the radial direction becomes strongly heterogeneous, rendering our interpretation of the fluidized bed as a continuous material inapplicable at such high $\dot{\gamma}_e$.

Flow regimes & non-monotonicity: Theoretical analysis

The rheological regimes observed are reminiscent of the rheological state diagram predicted by g-ITT (37), shown in the inset of Fig. 2A, and suggests to use g-ITT to analyze our data. In fact, we are going to calibrate the g-ITT constitutive relation with the measured data, taking shear banding into account. This will, in particular, allow us to obtain the true

shear rate, also in the shear thinning regime; by presenting the measured stress as a function of true shear rate, we deduce the constitutive relation of the fluidized bed under shear.

Granular Integration Through Transients. The g-ITT constitutive relation $\sigma(\dot{\gamma}/\omega_0|\Delta\varphi)/nT_0$ has been derived from first principles for a randomly driven fluid of monodisperse inelastic smooth hard spheres, characterized by a constant coefficient of restitution ε (see Methods for details). Its shape is controlled by the distance $\Delta\varphi_{\text{th}} = \varphi_g^{\text{MCT}}(\varepsilon) - \varphi$ to the granular glass transition $\varphi_g^{\text{MCT}}(\varepsilon)$, as determined by g-MCT, which depends on the coefficient of restitution ε (50). Moreover, the constitutive relation is only predicted up to an overall stress scale, nT_0 , equivalent to the ideal gas pressure in the unsheared granular fluid, and a rate scale, ω_0 , the collision frequency in the unsheared fluid. The g-ITT constitutive relation is therefore parametrized by the triple $(nT_0, \omega_0, \Delta\varphi_{\text{th}})$.

Qualitatively, g-ITT takes into account two key aspects of fluidized beds: (i) a finite structural relaxation time τ that diverges upon approaching the granular glass transition, and (ii) the fact that the granular temperature is set by the power balance between on one hand, the energy injected by fluidization, $u\Delta p/h$ (h being the bed height) and shear heating, $\sigma\dot{\gamma}$, and on the other hand, the energy dissipated in particle collisions. As a result, g-ITT predicts: Newtonian rheology for small Weissenberg numbers $Wi := \dot{\gamma}\tau \ll 1$, i.e., small densities and shear rates; shear thinning for $Wi \gg 1$; Bagnold scaling once shear heating dominates over fluidization at large shear rates (50). This is corroborated by the rheological regimes described above.

Shear Banding. The Taylor-Couette geometry enforces a radial variation of the stress $\sigma(r) \sim r^{-2}$ (see SI). For a measured stress only slightly above the stress plateau in the flow curve, this implies a large variation of the shear rate $\dot{\gamma}(r)$ in a small

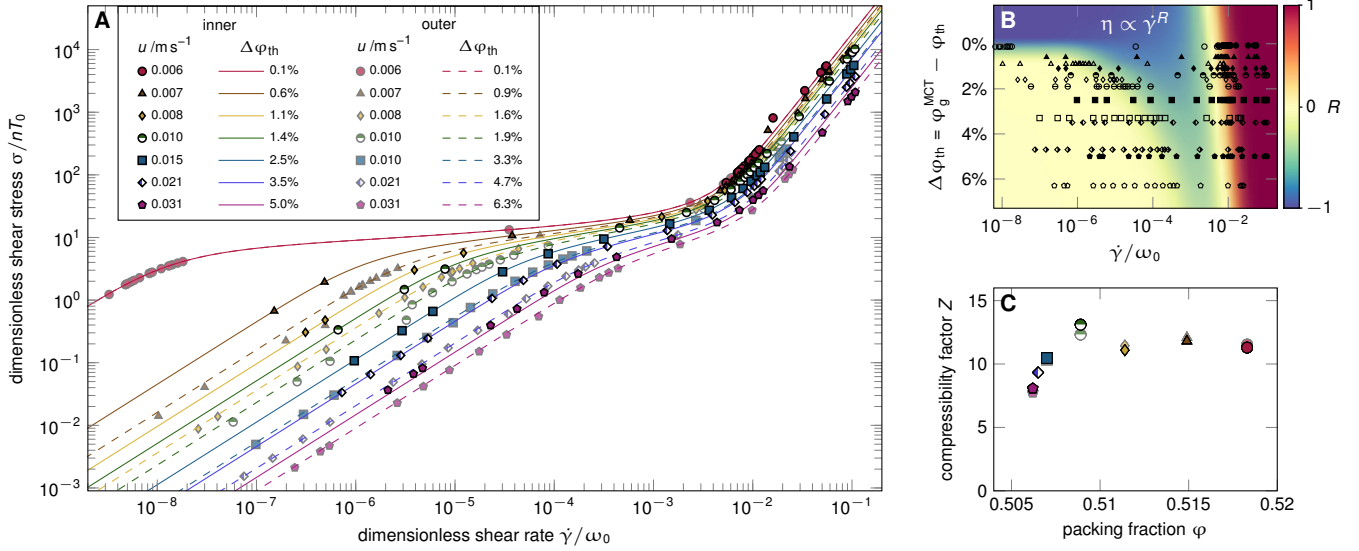


Fig. 4. Constitutive relation of an air-fluidized granular fluid. (A) Dimensionless shear stress σ/nT_0 as a function of dimensionless true shear rate $\dot{\gamma}/\omega_0$ on double-logarithmic axes. With this normalization, all temperature dependence is absorbed in the ideal gas pressure nT_0 and the collision frequency ω_0 (Fig. 3C) of the unsheared fluid. Symbols are the measurements (labeled by the fluidization velocity u ; for the corresponding packing fractions see Tab. 1) and lines are the GITT fits (Fig. 3). In this representation, there is only one fit parameter per curve, the distance to the granular glass transition $\Delta\varphi_{th}$ (Fig. 3D). (B) All the measurements (symbols) located in the rheological state diagram spanned by the dimensionless shear rate and $\Delta\varphi_{th}$. For the color code see Fig. 1. (C) Compressibility factor Z as a function of packing fraction calculated for the inner and outer region of the shear band showing that the fluidized bed features a unique equation of state. Same symbols as in A.

radial interval. Given the finite size particles, this is compatible with the interpretation of the non-monotonicity of $\sigma(\dot{\gamma}_e)$ as a manifestation of shear banding. More precisely, we assume that the sheared fluidized bed may radially split into an *inner* ($r < r^*$) and an *outer* region ($r > r^*$), which are in different states and with a discontinuous jump of the shear rate at the interface between the regions at $r = r^*$.

To account for shear banding in g-ITT, we allow for different sets of parameters in the outer and inner region of the shear cell, $(nT_0^o, \omega_0^o, \Delta\varphi^o)$, and $(nT_0^i, \omega_0^i, \Delta\varphi^i)$, respectively. Moreover, we assume no-slip boundary conditions, i.e., in terms of the local turning rate $U(r = R_i) \equiv U$, and $U(r = R_o) \equiv 0$. As we know the strain constants outside the shear banding regime, and local shear rates, $\dot{\gamma}(r)$, necessarily decrease from the inside to the outside, we fit the outer set of parameters to the low shear rate section and the inner set of parameters to the high shear rate section of the experimental flow curve, without regard to non-monotonous section at intermediate shear rates. However, the two branches of the constitutive equation needs to be unique for asymptotically large and small shear rates (see Fig. 3A for an example and Fig. S2 in SI for all fits). In the shear banding regime, we assume a coexistence of materials described by the two sets of parameters with an interface at a radial position $R_i < r^* < R_o$ (see Fig. 3B and Fig. S6), where r^* is determined by imposing continuity of stress and turning rate at the interface (see Methods for more details).

This procedure equips us with a lot of physical information, namely estimates for the granular temperature $T_0^{i,o}$ and the collision frequency $\omega_0^{i,o}$ (Fig. 3C), as well as theoretical estimates of the distance to the glass transition $\Delta\varphi^{i,o}$ (Fig. 3D). We will come back to those in the Discussion, but for now, let us focus on the shear rate profiles (Fig. 3B). In particular, we can read off the true shear rate at the inner cylinder $\dot{\gamma} = \dot{\gamma}(r = R_i)$. Plotting the latter against the effective shear rate $\dot{\gamma}_e$, as in

Fig. 3E, we observe that the fitting procedure conforms to the analytical strain constants at low and high shear rates, and that in the shear-banding regime, the relation is indeed highly non-linear. Although we only measure the stress at the inner cylinder, the stress at the outer cylinder, σ/δ^2 , is fixed by the force balance (see SI). With the corresponding shear rate $\dot{\gamma} = \dot{\gamma}(r = R_o)$, this allows us to extract a second flow curve from every measurement.

Given that we have obtained the relevant stress and rate scales, nT_0 and ω_0 , as well as the true shear rate $\dot{\gamma}$, we can replot the experimental flow curves in the proper dimensionless form, $\sigma(\dot{\gamma}/\omega_0)/nT_0$, using the true shear rate $\dot{\gamma}$ at both the inner and outer cylinder (Fig. 4A). Comparison to the g-ITT constitutive relation shows excellent agreement over many orders of magnitude in shear rate and stress. Note that in this representation, $\Delta\varphi_{th}$ is the single fit parameter per flow curve.

Discussion

The constitutive relation, $\sigma(\dot{\gamma})$, for an air-fluidized granular bed, featured in Fig. 4A, confirms that the manifold rheology of fluidized granular media, in fact, displays different rheological regimes: (i) For small Weissenberg number, $Wi \ll 1$, and negligible shear heating, the fluidized bed behaves as a Newtonian fluid with a viscosity η_N (Fig. 2 and Tab. 1) that diverges towards the granular glass transition at an effective packing fraction $\varphi_g = 0.519$. (ii) For higher shear rates, $Wi \gtrsim 1$, shear thinning and, eventually, at the granular glass transition $\varphi_g = 0.519$, a yield stress $\sigma_0 \approx 5$ Pa is observed as the shear rate exceeds the structural relaxation rate of the granular fluid. (iii) Once shear heating dominates, the rheology crosses over into Bagnold scaling, $\sigma = B\dot{\gamma}^2$, characterized by the Bagnold coefficient B (Fig. 2 and Tab. 1).

It is remarkable that the shape of the constitutive relations are solely controlled by $\Delta\varphi_{\text{th}}$, the distance to the granular glass transition. Note that, in order to cover all rheological regimes (Fig. 4B), measurements had to be performed consistently over many orders of magnitude in shear rate as well as shear stress, and over long times.

The transition from Newtonian to shear thinning at $Wi \sim 1$ is generic for dense suspensions (58, 60) as all suspensions (and, in fact, all fluids) feature a structural relaxation time τ . The location of the glass transition, φ_g , however, depends on the specifics of the particle interactions. While dense suspensions generally feature a shear thickening regime at high shear rates (58, 61), the Bagnold regime of the fluidized bed is probably of different origin. Rather than frictional or hydrodynamic interactions increasing the suspension’s viscosity as in the case of over-damped suspensions, the inertial granular fluidized bed features an increasing viscosity in the Bagnold regime due to the increasing granular temperature. The origin of this phenomenon is the decoupling of the granular temperature of the particles from the thermodynamic temperature of the suspending fluid that acts as a thermostat in more conventional suspension (38, 39). As we are studying air-fluidized glass beads, the viscosity η is always orders of magnitude larger than the air’s viscosity η_f , such that we observe no viscous-inertial transition (53, 54).

At first sight, our measured granular glass transition volume fraction $\varphi_g = 0.519$ is surprisingly low. For colloids in thermal equilibrium, $\varphi_g \simeq 0.57\text{--}0.58$ (62). G-MCT predicts that φ_g should increase further the more dissipative particles are (50). In particular, $\varphi_g^{\text{MCT}}(\varepsilon = 0.8) = 0.528$ compared to $\varphi_g^{\text{MCT}}(\varepsilon = 1) = 0.517$ with a well-known offset relative to experimental values. Note that φ_g is defined by the apparent divergence of the Newtonian viscosity at infinitesimal shear rate, $Wi \ll 1$. Here, the fluid’s structure has sufficient time to adapt to the shear flow, such that this is a phenomenon distinct from the proposed shear jamming behavior found at much higher packing fractions and for $Wi \gg 1$ (63). This adds further evidence, that a particulate fluid features a glass *and* a jamming transition (50, 64) rather than those two being different manifestations of a single transition (65).

Another manifestation of the low Stokes number, lubrication dominated particle interactions is the fact that the coefficient of restitution becomes strongly dependent on the Stokes number, $\varepsilon = \varepsilon(\text{St})$, (66, 67) and is no longer a material property of the glass beads. In particular, $\varepsilon = 0$ for $\text{St} \lesssim 10$. While at speeds on the order of m s^{-1} , glass spheres have $\varepsilon = \varepsilon_\infty \gtrsim 0.87$ (68), this implies that for the collision speeds relevant in the fluidized bed, the coefficient of restitution becomes strongly speed dependent, $\varepsilon = \varepsilon(v)$, with a typical value, $\varepsilon(v_0)$ much smaller than the high speed value ε_∞ . The data analysis in terms of g-ITT requires to specify an effective coefficient of restitution for the fluidized bed as a whole. The procedure works for any value of ε (see SI) with the result that the distance to the glass transition, $\Delta\varphi_{\text{th}}$, and the stress scale, nT_0 , only weakly depend on ε , whereas the rate scale, ω_0 , displays a marked dependence on ε .

Finally lubrication in combination with packing fractions far below jamming explains why we do not have to take into account inter-particle friction (69). While it is likely that residual frictional contacts renormalize the inferred system parameters to some extent, no new phenomenology appears that

isn’t captured by g-ITT, which assumes frictionless particles.

In the fully fluidized state, the granular temperatures increase with fluidization speed as expected. Typical particle speeds, inferred from the granular temperature T_0 are of the order but smaller than the fluidization velocity, $v_0 \lesssim u$, as expected (70). The opposite trend in the partially fluidized state hints at additional contributions to the stress scale nT_0 , likely borne by lasting particle contacts. Interestingly, the granular temperature in the inner region is significantly lower than in the outer region (Fig. 3C). This implies that strong shear somehow lowers the efficiency of fluidization, a phenomenon that certainly warrants further investigation.

Neither the stress scale, nT_0 , nor the rate scale, ω_0 , can be easily measured independently in a fluidized bed (70?, 71), and doing so is beyond the scope of the present study.

Predicting the expected collision frequency ω_0 suffers from the notorious lack of a good theoretical equation of state, $P(\varphi) = nT_0 Z(\varphi)$, giving the density dependence of the particle pressure P for the relevant packing fractions of order 0.5. For typical particle speeds, $v_0 \lesssim 2 \text{ cm s}^{-1}$, and assuming the Carnahan-Starling EOS, $Z_{\text{CS}}(\varphi)$ (72), we estimate $\omega_0 \lesssim 10 \text{ kHz}$ in line with the collision frequency extracted from the measurements (Fig. 3C). Given the significant ε -dependence of ω_0 , this led us to settle on an effective value for the coefficient of restitution $\varepsilon = 0.8$. For $\varepsilon = 0.8$, the parameters nT_0 and ω_0 assume reasonable values, as shown in Figs. 3 & 4. Note that both parameters reflect the transition from the partially, to the fully fluidized state which occurs at $u \approx 0.01 \text{ m s}^{-1}$ (Fig. 3C).

Although the parameters of the constitutive relation in the inner and outer region of the shear band differ (Fig. 3C), the equation of state of the unsheared fluidized bed, $Z(\varphi)$, must be unique throughout the sample. The compressibility factor, $Z(\varphi)$, can be estimated from the stress and rate scales (see Methods) for the inner and outer region. Fig. 4C shows reasonable data collapse, confirming a unique equation of state.

Note that for the present study we have explicitly taken a macroscopic point of view and have not used spatially resolved measurements. In particular, we have based our shear banding analysis on two simplifying assumptions: (i) that the inner and the outer region are both always in a sheared fluidized state, and (ii), that the regions are joined at a sharp interface. In the experiment, the interface will necessarily have a certain width on the particle scale and shear banding could also manifest itself in localized shear, leaving part of the sample unsheared. It would be interesting to measure particle motion in the bulk of the sample with sufficient temporal and spatial resolution to directly observe the flow profiles and compare them to the those determined here based on g-ITT. While challenging, we expect this to be in reach of recent advances in the field of *in-situ* visualization techniques (73–75). More demanding would be to achieve the resolution necessary to independently determine particle speeds or collision frequencies; measurements that would be very welcome, as well, in light of the role that those quantities play for the constitutive relation of a fluidized bed.

Apart from the radial separation into an inner and outer region, respectively, we have treated the sample as a spatially homogeneous material by time-averaging over the dynamics of the bubbles. We imagine that, eventually, our constitutive relation can be generalized from the *global* scale embraced here to a *local* – spatially and temporally resolved – contin-

uum description of the dynamic, bubbling fluidized bed (76) including start-up flows (12). Of particular conceptual interest would be a thorough analysis of the flow instabilities as has been done for molecular fluids (77, 78) but is, to date, mostly unexplored for granular fluids (79, 80).

Let us stress that our proposed constitutive relation does not contradict the $\mu(\mathcal{T})$ -rheology (35) or its generalizations to suspensions (81) but rather includes it (39, 82) and extends it beyond the Bagnold regime, where shear heating is no longer dominant and the fluidization flow becomes important.

In summary, we have validated and calibrated the g-ITT constitutive relation as a faithful model of the manifold rheology of air fluidized glass beads. On an explanatory level, this implies that fluidized beds will display Newtonian rheology if the shear rate is small compared to the intrinsic relaxation rate of the particle bed, $Wi \ll 1$, and shear heating can be neglected; they will display shear thinning for $Wi \gg 1$, as long as shear heating remains negligible; and finally, they will cross over to Bagnold scaling once shear heating dominates over fluidization. We hope that our work helps in understanding industrial and geophysical granular flows and can eventually lead to faithful continuum simulations (41) of large-scale granular applications.

Materials and Methods

Rheometry. All measurements presented were obtained using an Anton Paar MCR 302 rheometer with a powder cell and profiled inner cylinder (Fig. 5A), as described in Ref. (83). The geometry of the setup is an open-surface Taylor-Couette; important dimensions are given in Fig. 5B.

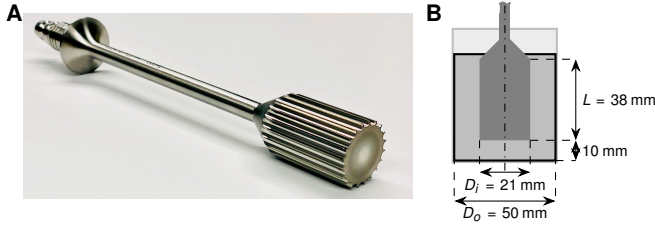


Fig. 5. Rheometry setup. (A) Profiled inner cylinder. (B) Important dimensions for the Taylor-Couette shear cell.

The rheometer records the torque \mathcal{M} as a function of the inner cylinder's rotation rate U . The torque can easily be converted to a stress at the inner cylinder, $\sigma = \mathcal{M}/\pi LR_i^2$. For purely Newtonian fluids in a Taylor-Couette geometry, the effective shear rate $\dot{\gamma} \equiv \dot{\gamma}_e = K_N 2\pi U$ is linearly related to the turning rate U by the strain constant

$$K_N = \frac{2\delta^2}{\delta^2 - 1}. \quad [3]$$

For all other rheologies, $\dot{\gamma}_e$, designates an effective shear rate, different from the true shear rate $\dot{\gamma}$.

Measurement Procedure. The flow curves presented in Fig. 1G were measured using the following experimental procedure: For a given fluidization velocity u , i.e. packing fraction φ , a desired apparent shear rate $\dot{\gamma}_e$ is imposed. Sufficient preshear is applied to reach a stationary state, as evidenced by reduced stress fluctuating around a constant mean value. Note that this takes a long time (up to strain $\gamma \approx 200$), as expected for a yield stress fluid (84). The mean value σ is obtained by averaging the stress over an additional strain window of twice the strain necessary to reach steady state.

The mean σ hence constitutes one data point in Fig. 1G, the error bar representing the standard deviation $\delta\sigma$ over the stationary state strain window. Between individual data points, the fluidization velocity u is increased to 0.05 m s^{-1} to erase any memory of the previous shear states. To check consistency, flow curves are measured successively in an upward and downward sweep in shear rate (respectively filled and empty marks in Figs. 1G, 2A and 3D). For each flow curve, each point $\sigma(u, \dot{\gamma}_e)$ is measured consecutively to ensure continuity in all flow curves, resulting in a measuring time per flow curve of around 200 h.

Particles. All measurements use a sample of mass $M = 125 \text{ g}$ of soda-lime glass spherical beads from Mo-Sci Corp, of diameter $63 \mu\text{m}$ to $75 \mu\text{m}$ (mean diameter $d = 69 \mu\text{m}$). The bulk material density is $\rho_b = 2.5 \text{ g cm}^{-3}$. The same glass beads were characterized in prior publications, see Refs. (31, 42).

Packing Fraction. The packing fraction is measured globally: it is calculated as $\varphi = M/\rho_b Ah$, where the sample volume Ah is obtained from the cross section of the shear cell, A , and the mean height h of the fluidized bed as determined by image analysis. The uncertainty in φ is dominated by systematic uncertainty in h which we estimate at $\pm 2.7\%$. For large air flow velocities u , fluctuation in h due to bubbling instabilities also becomes significant. The fluctuation magnitude is represented as error bars in Fig. 1B (standard deviation in φ for five independent repetition).

For the data presented in Fig. 1A and Fig. 1B, air flow velocity u and packing fraction φ are measured without the inner cylinder. The relation $\varphi(u)$ is obtained by fitting this data with the expression:

$$\varphi(u) = \varphi_0 + \frac{\varphi_\infty - \varphi_0}{1 + (u_0/(u - u_f))^2} \quad [4]$$

with $\varphi_\infty = 0.54$, $\varphi_0 = 0.506$, $u_0 = 0.0021 \text{ m s}^{-1}$ and $u_f = 0.0034 \text{ m s}^{-1}$. The fit is represented in Fig. 1B by a dashed gray line.

Fluidization Curves. The excess pressure Δp relative to ambient air pressure is measured at the base of the fluidized bed by a pressure transducer (mass flow controller from Bürkert).

Granular Integration Through Transients. To put it succinctly, g-ITT (37, 38) expresses the dimensionless shear stress $\hat{\sigma} = \sigma/nT$ of a dense fluid of dissipative smooth hard spheres as a generalized Green-Kubo integral

$$\hat{\sigma}(\text{Pe}) = \text{Pe} \sum_{\mathbf{q}} \int_0^\infty dt V_{\mathbf{q}\mathbf{q}(-t)} \Phi_{\mathbf{q}(-t)}^2(t), \quad [5]$$

where $\text{Pe} = \dot{\gamma}/\omega_c$ is a Péclet number. The physical intuition behind this equation is, that of all stress relaxation modes, the slowest one in dense fluids will be the density fluctuations encoded in the respective density correlator $\Phi_{\mathbf{q}}(t)$ (60). The stress-density coupling constant $V_{\mathbf{q}\mathbf{q}(-t)}$ is known explicitly (38). In addition to the explicit shear rate dependence of the above relation, the shear rate also affects the advection of the wave vectors, $\mathbf{q}(-t)$, and the density correlator $\Phi_{\mathbf{q}}(t)$ allowing for non-Newtonian rheology (38, 60). For granular fluids, as opposed to thermostatted colloidal suspensions, shear heating, $\sigma\dot{\gamma}$, elevates the granular temperature $T > T_0$ compared to the granular temperature T_0 of the unsheared granular fluid. The relation $T(\text{Pe})/T_0$ is known (38).

The g-ITT constitutive equation, $\hat{\sigma}(\text{Pe}) = \hat{\sigma}(\text{Pe}|\varphi, \epsilon)$, uses the packing fraction φ and the coefficient of restitution ϵ to uniquely characterize the granular fluid. Note, however, that the dominant effect of ϵ is in changing the glass transition density $\varphi_g = \varphi_g^{\text{MCT}}(\epsilon)$ (50) and only the distance to the glass transition $\Delta\varphi_{\text{th}} = \varphi_g^{\text{MCT}}(\epsilon) - \varphi$ matters for $\hat{\sigma}$. Therefore we regard the g-ITT constitutive relation,

$$\sigma(\text{Pe} \sqrt{T(\text{Pe})/T_0} | \Delta\varphi_{\text{th}})/nT_0 = \hat{\sigma}(\text{Pe} | \Delta\varphi_{\text{th}})T(\text{Pe})/T_0, \quad [6]$$

as characterized by the stress and rate scale, nT_0 , and $\omega_0 = \omega_c(T_0)$, respectively, as well as one more parameter, namely $\Delta\varphi_{\text{th}}$.

Fitting the Shear Band. We assume no-slip boundary conditions at the inner and outer cylinder and also at the shear band. Assuming two different g-ITT constitutive relations, $\sigma^i(\dot{\gamma}), \sigma^o(\dot{\gamma})$, at the inner and outer part of the shear cell, respectively, that meet at radial coordinate r^* , Eq. S2 (see SI) generalizes to a set of two equations

$$\int_{\sigma/\delta^2}^{\sigma^*} \frac{\dot{\gamma}^o(s) ds}{2s} = 2\pi U^* \quad [7]$$

$$\int_{\sigma^*}^{\sigma} \frac{\dot{\gamma}^i(s) ds}{2s} = 2\pi(U - U^*)$$

for the two unknowns, σ^* and U^* , the shear stress and turning rate at the shear band, respectively. Here $\dot{\gamma}^{i,o}(\sigma)$ are the inverse of the constitutive relations $\sigma^{i,o}(\dot{\gamma})$. Note that σ^* is uniquely related to the location r^* by the force balance (see SI).

We also need to determine the parameters of the g-ITT constitutive relations. As we do not *a priori* know the relation $\dot{\gamma}(U)$ in the non-monotonic middle part of the flow curves, we skip this part in the fitting procedure and assume the ideal strain constants only at the low and high shear rate ends of the flow curves. We fix the coefficient of restitution ϵ for all fits and then adjust the free parameters, $nT_0^{i,o}, \omega_0^{i,o}$, and $\Delta\varphi^{i,o}$ until we obtain a visually satisfying fit (see Fig. 3 and Figs. S2–5). Note that we require the collision frequencies to scale consistently with the temperatures, $\omega_0^i/\omega_0^o = \sqrt{T_0^i/T_0^o}$. This procedure fixes the constitutive relations $\sigma^{i,o}(\dot{\gamma})$, valid in the Bagnold and Newtonian regime, respectively. Next, we solve Eqs. 7 for the location of the shear band for those data points that deviate from the fit by either $\sigma^i(\dot{\gamma})$ or $\sigma^o(\dot{\gamma})$ alone.

By this procedure, we can associate every measurement $(U, \sigma(U))$, with a shear rate $\dot{\gamma}^i \equiv \dot{\gamma}^i(\sigma(U))$ at the inner cylinder and a shear rate $\dot{\gamma}^o \equiv \dot{\gamma}^o(\sigma(U)/\delta^2)$ at the outer cylinder. In the main part, we fix $\epsilon = 0.8$ and fit to the up-sweep measurements. For other choices of ϵ and for the down-sweep measurements, see the SI.

Determining the compressibility factor. The collision frequency of hard spheres can be written as a function of Z , $\omega_0 = \omega_0(Z, T_0) = 6\sqrt{T_0/\pi m}[Z(\varphi) - 1]/d$ (85), which can be inverted to obtain $Z^{i,o}(\omega_0^{i,o}, T_0^{i,o})$.

Data Availability. All data used in the paper is publicly available as SI.

ACKNOWLEDGMENTS. We are indebted to Dennis Schütz for designing the powder cell and for sharing unpublished measurements that were the starting point of this study. We thank Matthias Fuchs, Annette Zippelius, and Olivier Coquand for companionship in the long development of g-ITT and many more interesting discussions. We thank Thomas Voigtmann for sharing rheological insight and steady encouragement. W. T. K. acknowledges funding by the DFG through grant number KR4867/2 and the German Aerospace Centre through the project SciML. O. D'A. acknowledges funding by DLR/DAAD Research Fellowship 91647576 & ESA NPI-4000122340.

1. D Geldart, Types of gas fluidization. *Powder Technol.* **7**, 285–292 (1973).
2. D Kunii, O Levenspiel, eds., *Fluidization Engineering*. (Elsevier Science), 2 edition, (1991).
3. FA Zenz, *Fluidization Phenomena and Fluidized Bed Technology*, eds. ME Fayed, L Otten. (Springer US, Boston, MA), pp. 487–531 (1997).
4. M Horio, Fluidization in natural phenomena in *Reference Module in Chemistry, Molecular Sciences and Chemical Engineering*. (2017).
5. I Goldhirsch, Introduction to granular temperature. *Powder Technol.* **182**, 130–136 (2008).
6. S Bakhtiyarov, R Overfelt, Recent advances in the rheology of fluidized materials in *Advances in the Flow and Rheology of Non-Newtonian Fluids*, Rheology Series, eds. D Siginer, D De Kee, R Chhabra. Vol. 8, pp. 1399–1433 (1999).
7. O Roche, M Gilbertson, J Phillips, R Sparks, Experimental study of gas-fluidized granular flows with implications for pyroclastic flow emplacement. *Journal of Geophysical Research* **109** (2004).
8. A Kottlan, D Schütz, S Radl, Rheological investigations on free-flowing and cohesive powders in different states of aeration, using a ball measuring system. *Powder Tech.* **338**, 783–794 (2018).
9. ECP Breard, et al., Investigating the rheology of fluidized and non-fluidized gas-particle beds: implications for the dynamics of geophysical flows and substrate entrainment. *Granul. Matter* **24**, 34 (2022).

10. JA Dijkstra, GH Wortel, LTH van Dellen, O Dauchot, M van Hecke, Jamming, yielding, and rheology of weakly vibrated granular media. *Phys. Rev. Lett.* **107**, 108303 (2011).
11. Z Zhang, Y Cui, DH Chan, KA Taslagyan, DEM simulation of shear vibrational fluidization of granular material. *Granul. Matter* **20**, 71 (2018).
12. A Gnoli, A Lasanta, A Sarracino, A Puglisi, Unified rheology of vibro-fluidized dry granular media: From slow dense flows to fast gas-like regimes. *Sci. Reports* **6**, 38604 (2016).
13. HJ Melosh, Dynamical weakening of faults by acoustic fluidization. *Nature* **379**, 601–606 (1996).
14. JW Conrad, J Melosh, The rheology of acoustically fluidized sand in *AGU Fall Meeting Abstracts*. Vol. 2013, pp. P41F–1986 (2013).
15. C Wilson, The role of fluidization in the emplacement of pyroclastic flows. 2: Experimental results and their interpretation. *J. Volcanol. Geotherm. Res.* **20**, 55–84 (1984).
16. K Kelfoun, P Samaniego, P Palacios, D Barba, Testing the suitability of frictional behaviour for pyroclastic flow simulation by comparison with a well-constrained eruption at tungurahua volcano (ecuador). *Bull. Volcanol.* **71**, 1057–1075 (2009).
17. I Eames, M Gilbertson, Mixing and drift in gas-fluidised beds. *Powder Technol.* **154**, 185–193 (2005).
18. J Werther, *Fluidized-Bed Reactors*. (John Wiley & Sons, Ltd), (2007).
19. M Menéndez, J Herguido, A Bérard, GS Patience, Experimental methods in chemical engineering: Reactors—fluidized beds. *The Can. J. Chem. Eng.* **97**, 2383–2394 (2019).
20. R Dhurandhar, JP Sarkar, B Das, The recent progress in momentum, heat and mass transfer studies on pneumatic conveying: a review. *Heat Mass Transf.* **54**, 2617–2634 (2018).
21. GL Matheson, WA Herbst, PH Holt, Characteristics of fluid-solid systems. *Ind. Eng. Chem.* **41**, 1098–1104 (1949).
22. T Hagyard, AM Sacerdote, Viscosity of suspensions of gas-fluidized spheres. *Ind. Eng. Chem. Fundamentals* **5**, 500–508 (1966).
23. N Maeno, K Nishimura, Y Kaneda, Viscosity and heat transfer in fluidized snow. *J. Glaciol.* **26**, 263–274 (1980).
24. E Koos, E Linares-Guerrero, ML Hunt, CE Brennen, Rheological measurements of large particles in high shear rate flows. *Phys. Fluids* **24**, 013302 (2012).
25. P van den Leeden, GJ Bouwhuis, Tentative rules for shearing stresses in particulate fluidized beds. *Appl. Sci. Res.* **10**, 78–80 (1961).
26. GI Tardos, MI Khan, DG Schaeffer, Forces on a slowly rotating, rough cylinder in a couette device containing a dry, frictional powder. *Phys. Fluids* **10**, 335–341 (1998).
27. DM Hanes, DL Inman, Observations of rapidly flowing granular-fluid materials. *J. Fluid Mech.* **150**, 357–380 (1985).
28. K Schürgerl, M Merz, F Fetting, Rheologische eigenschaften von gasdurchströmten fließbettsystemen. *Chem. Engng. Sci.* **15**, 1–38 (1961).
29. EF Hobbel, B Scarlett, Measurement of the flow behaviour of aerated and fluidised powders using a rotating viscometer. *Part. & Part. Syst. Charact.* **2**, 154–159 (1985).
30. J Gottschalk, Rheological study of loosened bulk granular materials. *Part. & Part. Syst. Charact.* **3**, 168–173 (1986).
31. I Mishra, P Liu, A Shetty, CM Hrenya, On the use of a powder rheometer to probe defluidization of cohesive particles. *Chem. Eng. Sci.* **214**, 115422 (2020).
32. AB Young, A Shetty, ML Hunt, Flow transitions and effective properties in an annular couette rheometer for gas fluidized beds and liquid-solid suspensions. *submitted to J. Fluid Mech.* (2021).
33. RA Bagnold, Experiments on a gravity-free dispersion of large solid spheres in a newtonian fluid under shear. *Proc. Royal Soc. Lond. Ser. A* **225**, 49–63 (1954).
34. G Lois, A Lemaitre, JM Carlson, Numerical tests of constitutive laws for dense granular flows. *Phys. Rev. E* **72**, 051303 (2005).
35. GDR MiDi, On dense granular flows. *Eur. Phys. J. E* **14**, 341–365 (2004).
36. V Francia, LAA Yahia, R Ocone, A Ozel, From quasi-static to intermediate regimes in shear cell devices: Theory and characterisation. *KONA Powder Part. J.* p. 2021018 (2021).
37. WT Kranz, F Frahsa, A Zippelius, M Fuchs, M Sperl, Rheology of inelastic hard spheres at finite density and shear rate. *Phys. Rev. Lett.* **121**, 148002 (2018).
38. WT Kranz, F Frahsa, A Zippelius, M Fuchs, M Sperl, Integration through transients for inelastic hard sphere fluids. *Phys. Rev. Fluids* **5**, 024305 (2020).
39. A Lemaitre, JN Roux, F Chevoir, What do dry granular flows tell us about dense non-brownian suspension rheology? *Rheol. Acta* **48**, 925–942 (2009).
40. É Guazzelli, O Pouliquen, Rheology of dense granular suspensions. *J. Fluid Mech.* **852** (2018).
41. J Wang, Continuum theory for dense gas-solid flow: A state-of-the-art review. *Chem. Engng. Sci.* **215**, 115428 (2020).
42. CQ LaMarche, P Liu, KM Kellogg, CM Hrenya, Fluidized-bed measurements of carefully-characterized, mildly-cohesive (group a) particles. *Chem. Engng. J.* **310**, 259–271 (2016).
43. JR Grace, B Leckner, J Zhu, Y Cheng, *Fluidized Beds*, ed. CT Crow. (CRC Press), pp. 5–71 (2008).
44. JM Valverde, A Ramos, A Castellanos, P Keith Watson, The tensile strength of cohesive powders and its relationship to consolidation, free volume and cohesivity. *Powder Technol.* **97**, 237–245 (1998).
45. R Jackson, *The dynamics of fluidized particles*. (Cambridge University Press), (2000).
46. WT Kranz, O Coquand, O D'Angelo, Understanding dense granular flow from first principles. *Sci. Talks* **3**, 100049 (2022).
47. IM Krieger, TJ Dougherty, A mechanism for non-newtonian flow in suspensions of rigid spheres. *Trans. Soc. Rheol.* **3**, 137–152 (1959).
48. C Song, P Wang, HA Makse, A phase diagram for jammed matter. *Nature* **453**, 629–632 (2008).
49. AR Abate, DJ Durian, Approach to jamming in an air-fluidized granular bed. *Phys. Rev. E* **74**, 031308 (2006).
50. WT Kranz, M Sperl, A Zippelius, Glass transition for driven granular fluids. *Phys. Rev. Lett.* **104**, 225701 (2010).
51. A Seguin, O Dauchot, Experimental evidence of the gardner phase in a granular glass. *Phys. Rev. Lett.* **117**, 228001 (2016).
52. Y Forterre, O Pouliquen, Flows of dense granular media. *Annu. Rev. Fluid Mech.* **40** (2008).

53. Y Madraki, et al., Shear thickening in dense non-brownian suspensions: Viscous to inertial transition. *J. Rheol.* **64**, 227–238 (2020).
54. F Tapia, M Ichihara, O Pouliquen, E Guazzelli, Viscous to inertial transition in dense granular suspension. *Phys. Rev. Lett.* **129**, 078001 (2022).
55. JT Jenkins, Dense inclined flows of inelastic spheres. *Granul. Matter* **10**, 47–52 (2007).
56. NA Spenley, XF Yuan, ME Cates, Nonmonotonic constitutive laws and the formation of shear-banded flows. *J. Phys. II* **6**, 551–571 (1996).
57. SM Fielding, Complex dynamics of shear banded flows. *Soft Matter* **3**, 1262–1279 (2007).
58. JJ Stickel, RL Powell, Fluid mechanics and rheology of dense suspensions. *Annu. Rev. Fluid Mech.* **37**, 129–149 (2005).
59. HA Barnes, MF Edwards, LV Woodcock, Applications of computer simulations to dense suspension rheology. *Chem. Eng. Sci.* **42**, 591–608 (1987).
60. M Fuchs, ME Cates, Theory of nonlinear rheology and yielding of dense colloidal suspensions. *Phys. Rev. Lett.* **89**, 248304 (2002).
61. E Brown, HM Jaeger, Shear thickening in concentrated suspensions: phenomenology, mechanisms and relations to jamming. *Reports on progress physics* **77** (2014).
62. W van Meegen, Crystallisation and the glass transition in suspensions of hard colloidal spheres. *Transp. Theory Stat. Phys.* **24**, 1017–1051 (1995).
63. D Bi, J Zhang, B Chakraborty, RP Behringer, Jamming by shear. *Nature* **480**, 355–358 (2011).
64. P Charbonneau, J Kurchan, G Parisi, P Urbani, F Zamponi, Glass and jamming transitions: From exact results to finite-dimensional descriptions. *Annu. Rev. Condens. Matter Phys.* **8**, 265–288 (2017).
65. AJ Liu, SR Nagel, Jamming is not just cool any more. *Nature* **396**, 21–22 (1998).
66. P Gondret, M Lance, L Petit, Bouncing motion of spherical particles in fluids. *Phys. Fluids* **14**, 643–652 (2002).
67. FL Yang, ML Hunt, A mixed contact model for an immersed collision between two solid surfaces. *Phil. Trans. Royal Soc. A* **366**, 2205–2218 (2008).
68. A Lorenz, C Tuozzolo, MY Louge, Measurements of impact properties of small, nearly spherical particles. *Exp. Mech.* **37**, 292–298 (1997).
69. E DeGiuli, JN McElwaine, M Wyart, Phase diagram for inertial granular flows. *Phys. Rev. E* **94**, 012904 (2016).
70. MJ Biggs, et al., Granular temperature in a gas fluidized bed. *Granul. Matter* **10**, 63–73 (2008).
71. GD Cody, DJ Goldfarb, GV Storch Jr, AN Norris, Particle granular temperature in gas fluidized beds. *Powder Tech.* **87**, 211–232 (1996).
72. NF Carnahan, KE Starling, Equation of state for nonattracting rigid spheres. *J. Chem. Phys.* **51**, 635–636 (1969).
73. J Baker, F Guillard, B Marks, I Einav, X-ray rheography uncovers planar granular flows despite non-planar walls. *Nat. Commun.* **9**, 5119 (2018).
74. A Rosato, K Windows-Yule, Chapter 3 – Investigative approaches I: Experimental imaging techniques in *Segregation in Vibrated Granular Systems*, eds. A Rosato, K Windows-Yule. (Academic Press), pp. 37–74 (2020).
75. R Stannarius, Magnetic resonance imaging of granular materials. *Rev. Sci. Instruments* **88**, 051806 (2017).
76. Q Guo, et al., Dynamically structured bubbling in vibrated gas-fluidized granular materials. *Proc. Natl. Acad. Sci.* **118**, e2108647118 (2021).
77. GI Taylor, Stability of a viscous liquid contained between two rotating cylinders. *Philos. Transactions Royal Soc. Lond.* **223**, 289–343 (1923).
78. JT Stuart, Taylor-vortex flow: a dynamical system. *SIAM Rev.* **28**, 315–342 (1986).
79. SL Conway, T Shinbrot, BJ Glasser, A Taylor vortex analogy in granular flows. *Nature* **431**, 433–437 (2004).
80. KP Krishnaraj, PR Nott, A dilation-driven vortex flow in sheared granular materials explains a rheometric anomaly. *Nat. Comm.* **7**, 1–8 (2016).
81. F Boyer, É Guazzelli, O Pouliquen, Unifying suspension and granular rheology. *Phys. Rev. Lett.* **107**, 188301 (2011).
82. O Coquand, M Sperl, WT Kranz, Integration through transients approach to the $\mu(I)$ rheology. *Phys. Rev. E* **102**, 032602 (2020).
83. H Salehi, D Sofia, D Schütz, D Barletta, M Poletto, Experiments and simulation of torque in anton paar powder cell. *Part. Sci. Technol.* **36**, 501–512 (2018).
84. PCF Møller, A Fall, D Bonn, Origin of apparent viscosity in yield stress fluids below yielding. *Eur. Lett.* **87**, 38004 (2009).
85. T Pöschel, S Luding, eds., *Granular Gases*. (Springer-Verlag, Berlin Heidelberg), (2001).